

# Silicon on-chip Electro-optic Modulation With Ito Film Stacks

Evgeniy S. Lotkov (✉ [lotevg@bmstu.ru](mailto:lotevg@bmstu.ru))

Bauman Moscow State Technical University

Alexander S. Baburin

Bauman Moscow State Technical University

Ilya A. Ryzhikov

Institute for Theoretical and Applied Electromagnetics RAS

Olga S. Sorokina

Bauman Moscow State Technical University

Anton I. Ivanov

Bauman Moscow State Technical University

Alexander V. Zverev

Bauman Moscow State Technical University

Igor V. Bykov

Institute for Theoretical and Applied Electromagnetics RAS

Alexander V. Baryshev

Dukhov Automatics Research Institute, (VNIIA)

Yuri V. Panfilov

Bauman Moscow State Technical University

Ilya A. Rodionov

Bauman Moscow State Technical University

---

## Research Article

**Keywords:** Indium tin oxide (ITO), amorphous, heterogeneously crystalline, ITO

**Posted Date:** September 17th, 2021

**DOI:** <https://doi.org/10.21203/rs.3.rs-885537/v1>

**License:**   This work is licensed under a Creative Commons Attribution 4.0 International License.

[Read Full License](#)

---

# Abstract

Indium tin oxide (ITO) platform is one of the promising solutions towards state-of-the-art integrated optical modulators for silicon photonics applications. We demonstrate the way to obtain both high extinction ratio and low insertion loss electro-optic modulation with ITO-based film stack. By investigating e-beam evaporated 20 nm-thick ITO films with amorphous, heterogeneously crystalline, homogeneously crystalline with hidden coarse grains and pronounced coarsely crystalline structure, a low carrier concentration (from  $1 \cdot 10^{20}$  to  $2 \cdot 10^{20}$   $\text{cm}^{-3}$ ) is achieved. The mechanism of oxygen migration in ITO film crystallization is proposed based on morphological features observed under low-energy growth conditions. We compare three electro-optic modulator active elements (current-voltage and optical characteristics) and reach strong ITO dielectric permittivity variation induced by charge accumulation/depletion ( $\Delta n = 0.199$ ,  $\Delta k = 0.240$  at  $\lambda = 1550\text{nm}$  under  $\pm 16\text{V}$ ). Our simulations and experimental results demonstrate the unique potential to create integrated GHz-range electro-optical modulators with sub-db losses.

## Introduction

There are several promising fields of integrated photonics like quantum computing, LIDARs, high-performance datacenters, neuromorphic computing and precision optical spectroscopy [1–5], which can extremely benefit when low loss integrated optical modulators appear. A number of optical modulator implementations based on various physical effects have been already demonstrated (Table 1). The device quality is generally determined by high speed, low losses, small footprint, manufacturing and integration flexibility. One of the most frequently used modulator types is a lithium niobate modulator based on Pockels effect [6, 7]. It demonstrates low propagation losses (down to 0.1 dB) and high modulation speed (more than 40 GHz). The key remaining challenge of lithium niobate modulators is a very long active element length of about 2 millimeters. Another optical modulator is based on the free-carrier plasma dispersion effect (FCPD), where the active element is either p-n or p-i-n junction. Such modulators are based on charge carrier concentrations change [8, 9]. They show high speed (more than 30 GHz) and medium footprint (active element length is 100–2000  $\mu\text{m}$ ). However, the propagation loss is significantly higher than that of lithium niobate. Organic electro-optical materials are also used for high-performance devices fabrication based on the Pockels effect [10, 11]. They could provide both high speed (more than 40 GHz) and small footprint (active length down to 5  $\mu\text{m}$ ), but show high propagation losses (around 2.5 dB in the active part). Another optical modulators type based on Franz-Keldysh effect and quantum-confined Stark effect are implemented mostly in InP or GeSi structures [12]. These modulators have high speed (more than 40 GHz), low loss (about 1 dB in the active part) and medium footprint. However, they require high complexity of manufacturing and integration. In the last 10 years, high interest is devoted to optical modulators based on the change of dielectric constant in transparent conductive oxides (TCO), such as indium tin oxide (ITO) [13–16]. Free carriers accumulation (depletion) in ITO provides small device footprint (active element length of about 5  $\mu\text{m}$ ) and low propagation loss (down to 0.5 dB). Their modulation frequency has been experimentally approved up to 1 GHz, but higher speed

could be reached [17]. Efficiency and propagation loss in such modulators are generally determined by TCO film properties. TCO-based devices demonstrate a trade-off between light propagation losses, size and modulation rate, making them one of the most promising solutions. Moreover, all the materials used in these devices are well compatible with planar silicon technology. One of the most widely used TCO thin films is indium tin oxide. Its permittivity depends on the carrier concentration and is described by the Drude–Lorentz model [18], thus, both real and imaginary part of thin film can be tuned [19], which makes ITO a reasonable choice for modulator active element implementation. Optical modulators based on thin film optical properties change effect could be realized as a hybrid waveguide, which represents a metal-oxide-semiconductor (MOS) capacitor with a built-in thin ITO layer. When an electrical potential is applied to active element, the charge accumulation layer is formed on the oxide/ITO interface where carrier concentration is significantly higher. The light mode localized in this sub-um volume is absorbed [13, 14] or changes the phase [15, 16]. One of the key points for high-performance optical modulators is ITO thin film carrier concentration, which strongly affects light propagation loss and modulation depth. We simulated an ITO-based optical modulator and found that with a carrier concentration in the ITO film in the range of  $0.5$  to  $2 \times 10^{20} \text{ cm}^{-3}$  (see Supplementary), both the optimal device length and the minimum propagation loss can be achieved. ITO thin films with controllable carrier concentration are deposited with high-energy PVD methods such as ion beam deposition [15, 16], magnetron sputtering [23, 24] and pulsed laser deposition [22] to avoid the following film annealing, which leads to strong carrier concentration increase. Ion-beam assisted electron beam evaporation deposition (IBAD) without annealing [25, 26] is also used, but morphology and extinction coefficient of such thin films have not been investigated for ultrathin layers.

Table 1  
Comparison of electro-optical modulators implementations.

| Modulator type                     | L, um    | Vswitch, V | ER, dB  | Speed, GHz | IL (modulation area), dB |
|------------------------------------|----------|------------|---------|------------|--------------------------|
| p-i-n and p-n junction based (MZM) | 100–2000 | 1.8–6.5    | 3.1–7.5 | > 30       | 1.5–6                    |
| Lithium niobate based (MZM)        | 50–5000  | 2.3–9      | < 20    | > 40       | 0.1–4                    |
| InP based (MZM, EAM)               | ~ 300    | 1.5–3      | < 25    | 1.5–40     | ~ 1                      |
| NLM based (MZM)                    | 5–1500   | 3.3–4      | 4–5     | > 40       | 2.5–8                    |
| TCO based (MZM, EAM)               | 5–32     | 3–32       | 2.1–5   | > 1        | 0.5–6                    |

In this work, we propose ion-beam assisted e-beam evaporation followed by annealing which provides a very stable and controlled carrier concentration of ITO films. Opposed to sputtering and ion beam deposition the proposed IBAD deposition process is characterized by lower energies avoiding intensive crystallization and formation of transition layer [27]. E-beam thin films evaporation is very flexible; it allows deposition in UHV conditions with quite a small amount of extremely pure materials. Additionally,

ion assistance during evaporation process and following annealing in inert atmosphere [28] makes it possible to improve the film crystalline structure and properties without a significant increase in the carrier concentration. In order to estimate the electro-optical effect we fabricated and experimentally compared MOS capacitors based on evaporated ITO films, which are pretty similar to active element of electro-optical modulators. We investigate its current-voltage characteristics and analyze the electro-optical effect in accumulation/depletion layers using spectroscopic ellipsometry [20–22]. With this experimental data set we calculated electro-optical modulator parameters using COMSOL.

## Methods

**ITO deposition.** ITO thin films were deposited on prime-grade oxidized doped Si(100) substrates ( $10\text{--}20\ \Omega\cdot\text{cm}$ ) using 10kW e-beam evaporator (Angstrom Engineering) with a base pressure lower than  $3\times 10^{-8}$  Torr. We first cleaned the wafers in a 2:1 sulfuric acid: hydrogen peroxide solution ( $80^\circ\text{C}$ ), followed by further cleaning in isopropanol to eliminate organics. Next, we placed the wafers in 49% hydrofluoric acid for approximately 20 s to remove the native oxide layer. All films were grown using 5N (99.999%) pure ITO pieces ( $\text{In}_2\text{O}_3$  – 90%, SnO – 10%). Films were deposited with rate of  $2\ \text{\AA}/\text{s}$  measured with quartz monitor at approximate source to substrate distance of 30 cm. Thickness of all ITO thin films was  $20 \pm 2\ \text{nm}$ . Ion assistance (accelerating voltage 70 V) and deposition on substrate with elevated temperature ( $150^\circ\text{C}$ ) were made to study its effects on thin film structure, resistivity and carrier concentration. Subsequent annealing was carried out in an argon atmosphere for 20 minutes.

**Resistivity measurement.** For resistivity measurement four-point probe method was used by four-probe surface resistance measurement system ResMap 178 (CDE).

**Scanning electron microscopy.** In order to check the quality and uniformity of the deposited layers ITO films surfaces immediately after deposition were investigated by means of a scanning electron microscope Zeiss Merlin with a Gemini II column. All SEM images were obtained using in-lens detector and the accelerating voltage 5 kV and working distance from the sample to detector from 1 to 4 mm. Magnifications 3000, 7000, 15000 and 50000 were used to fully analyze samples.

**Electron backscatter diffraction.** Crystallinity of the obtained ITO thin films was studied by electron backscatter diffraction (EBSD) by Nordlys-II S electron back-scattering detector (Oxford Instruments) at an accelerating voltage of 10 keV at working distance of 12.5 mm and the sample tilt angle in the microscope chamber of  $70^\circ$ . The AZtec 3.3 software was used for the area analyze. In the work Quaas et al. [39] XRD analysis of ITO films showed In and  $\text{In}_2\text{O}_3$  phases, while Sn and  $\text{SnO}_x$  phases were not detected (it is assumed that the phases are embedded in the In /  $\text{In}_2\text{O}_3$  lattice). Here, for the analysis, we also used the  $\text{In}_2\text{O}_3$  phases (lattice – cubic low; space group – 206; diffraction symmetry class:  $m^{-3}$ , a, b, c = 10.12 Å, Alpha –  $90^\circ$ , Beta –  $90^\circ$ , Gamma –  $90^\circ$ ). Search for  $\text{SnO}_x$  phases did not return any results.

**Stylus profilometry.** The stylus profiler KLA Tencor P17 (with Durasharp 38-nm tip radius stylus) was used. All measurements were done by using 0.5 mg tapping strength, scan rate was  $2\ \mu\text{m}/\text{s}$  and the

scanned line length was 20  $\mu\text{m}$ .

**Active element layer stack fabrication.** For multilayer stack fabrication, ITO thin films areas of 5  $\text{mm}^2$  square were formed on oxidized silicon substrates using shadow mask deposition technique. Aluminum or silver electrodes were then deposited at room temperature (deposition parameters could be found elsewhere [40]) on the surface of ITO and Si (Fig. 1b) to provide better contact during electrical testing. The sample was connected to power supply unit using a self-made contacting tool installed on the ellipsometer stage (Fig. 1b). For the optical measurements, an additional focusing to the microspot of about 200  $\mu\text{m}$  was used. Experimental stands based on the Sentech SE 800 PV and Woollam V-VASE ellipsometers were developed. It allows measuring a change of ellipsometric parameters  $\psi$  and  $\Delta$  for the MOS structures and thin films optical properties under applied voltage.

## Results And Discussion

**ITO thin films investigation.** The key technology for the state-of-the-art ITO-based on-chip electro-optic modulator is ITO thin film with a strong compromise between carrier concentration and optical properties. Using typical value of ITO films carrier mobility ( $15 \text{ cm}^2/(\text{V}\cdot\text{s})$ ) [18, 32], we calculated ( $\rho = 1/\mu_c N_c e$ ) its resistivity which has to be in the range from 2 to  $8 \times 10^3 \Omega\cdot\text{cm}$ . First, we compared resistivity, optical properties and surface morphology (Fig. 1) of four 20 nm-thick ITO films: 1) high temperature IBA e-beam evaporation (film1); 2) room temperature IBA e-beam evaporation with following 300C annealing (film2); 3) high temperature IBA e-beam evaporation with following 300C annealing (film3); 4) room temperature e-beam evaporation with following 300°C annealing (film4). We observe strong variation in films resistivity measured by the four-probe method with respect to evaporation technology and annealing parameters (Fig. 1a, detailed description see Supplementary). The resistivity of ITO film deposited at room temperature without annealing (not shown) is more than  $10^1 \Omega\cdot\text{cm}$ , which indicates insufficient film crystallization and large amount of interstitial non-activated oxygen [29–31]. All the evaporated ITO films are ultra-flat with the RMS film surface roughness  $0.7 \pm 0.2 \text{ nm}$ . Analyzing high-quality SEM images of the films one can observe strong texture growth for annealed films (Fig. 1d, films 2–4) and homogeneous microstructure for the film evaporated under elevated temperature without subsequent annealing.

Optical constants of the films 1–3 are measured in the wavelength range from 400 to 1600 nm (Fig. 1b, 1c); film4 was not studied as the carrier concentration of this film was too high. Evidently, film1 has much higher absorption in the whole visible range (Fig. 1c), which can be explained by low film crystallization during evaporation. Strong texture of film2 indicates an intense crystallization process that results in the lowest absorption over the entire wavelength range. ITO film3 also has a strong crystalline texture (Fig. 1d) and relatively low extinction coefficient in the visible region. The carrier mobility of film3 is higher than for films 1 and 2 (calculated based on the Drude–Lorentz model and spectroscopic ellipsometry experimental results  $\approx 30$  and  $11\text{--}15 \text{ cm}^2/(\text{V}\cdot\text{s})$ ), which can be explained by a less defective crystalline structure (see Discussion). The carrier concentrations for ITO films 1–3 is calculated as  $N_c = 1/\rho e \mu$  and equals to  $3.4 \cdot 10^{20} \text{ cm}^{-3}$ ,  $3.7 \cdot 10^{20} \text{ cm}^{-3}$  and  $5.5 \cdot 10^{20} \text{ cm}^{-3}$  correspondingly. According to previously

reported data [18] films 1 and 2 are promising candidates for electro-optic modulators in both n-dominant (Mach-Zehnder) and k-dominant (electro-absorption) regions. The value for

film3 is the closest to epsilon-near-zero point (ENZ) at  $\lambda = 1550$  nm (Figs. 1b, 1c, Drude-Lorentz model for ENZ). This type of ITO films can be used for electro-optic elements which require dielectric constant switching through ENZ point [33, 34].

However, low-loss n-dominant electro-optic modulator requires ITO films with higher resistance values (from  $2 \cdot 10^{-3}$  to  $8 \cdot 10^{-3} \Omega \cdot \text{cm}$ ). We clearly observe that ITO films resistance is directly related to films crystalline structure and morphology. We investigate two methods to control ITO films resistance: 1) Ar/O<sub>2</sub> gas mixture variation during IBAD evaporation with subsequent annealing; 2) annealing with different temperatures. Due to minimum extinction coefficient and acceptable resistivity, we choose a deposition recipe for film2 for further improvement. We studied two ITO films evaporated under room temperature (IBAD in Ar/O<sub>2</sub> mixture with 2 sccm and 4 sccm Ar flow) without and with subsequent 20 minutes annealing in an argon atmosphere at 300°C (Fig. 1e). It can be seen that films annealing allows controllably reduce their resistance to the desired region. ITO films with relatively high resistance (more than  $10^{-2} \Omega \cdot \text{cm}$ ) have an amorphous or nanocrystalline structure (Fig. 1e, no crystalline phases were found during SEM EBSD analysis). Films with relatively low

resistance (less than  $10^{-3} \Omega \cdot \text{cm}$ ) have a crystalline structure (grains with hidden boundaries were detected by SEM EBSD diffraction analysis). Films with middle resistance (from  $10^{-3}$  to  $10^2 \Omega \cdot \text{cm}$ ) have a crystalline structure with the inclusions of amorphous phases. Finally, we investigated the dependence of ITO films resistance and crystalline structure (room temperature IBAD in Ar/O<sub>2</sub> mixture (Ar flow = 4 sccm and O<sub>2</sub> flow = 12 sccm)) on annealing temperature and atmosphere (Fig. 2a). One can observe that ITO film annealed at 300°C stays amorphous, while increasing the temperature by only 20°C immediately initializes the crystallization. We marked stepwise crystallization behavior which leads a well-defined crystalline ITO structure when annealed temperature becomes more than 500°C. Under higher temperatures (more than 1000°C) the films are damaged, melt and break into islands under surface forces. It should be noted that annealing in the atmosphere with a small fraction of oxygen increases resistance significantly (Fig. 2a, light blue point). In this case, the film

has a crystalline structure, in contrast to the partial crystallization (Fig. 1e), which is observed for the films with suitable resistivity annealed in a pure argon atmosphere. SEM EBSD analysis (Fig. 2b) demonstrates that increasing the annealing temperature in argon atmosphere (points 1 to 3) leads to increasing the pole density of reflecting planes orientations of ITO films (see inverse pole figures (IPF)). It indicates the appearance of preferred grains orientations in ITO films. Moreover, for the films annealed in oxygen-diluted atmosphere (point 4) the orientation of the grains is different which gives additional ways to control ITO films properties.

We assume that IBAD films have some structural crystalline features and represent chemically heterogeneous systems before annealing. Since the energy in IBAD processes is higher, crystal nuclei

formation occurs during evaporation process (which is confirmed by EBSD analysis for non-annealed thin film – Fig. 3c). Based on the SEM image analysis (Fig. 3a, 3b) one can assume that during annealing the crystallization front propagation from nucleus along the growth channel occurs along preferred orientations similar to the processes occurring during the liquid- phase epitaxy [36]. In this case, the front movement can form opposite diffusion flow which is perpendicular to the growing surface (Fig. 3d). In other words, during ITO crystallization a depletion zone appears, where oxygen diffuses to build a crystal lattice. SEM images (Figs. 3a, 3b) show 2–6 channels radially emerging from each central point, which can be oxygen diffusion channels.

We observed that annealing of ITO films deposited without ion assistance causes greater resistance decrease (Fig. 1a). The part of the ITO structure crystallizes during evaporation (Fig. 3c). For ion-assisted processes, oxygen atoms and ions outside the crystal lattice are embedded into the volume of the film [29–31]. This affects further crystallization during annealing when oxygen annihilation with vacancies occurs [35]. Wherein the crystalline phase is more localized in the films evaporated with ion-assistance.

Thus, our deposition technique involves the usage of low energies and higher oxygen concentrations, which distinguishes it from other methods described in recent scientific papers [25, 26]. These conditions favor the formation of a non-crystalline film, as evidenced by the low carrier concentration ( $N_c < 4 \cdot 10^{18} \text{ cm}^{-3}$ ). The films deposited at higher energy and lower oxygen concentration without further annealing show higher carrier concentrations ( $N_c > 1 \cdot 10^{19} \text{ cm}^{-3}$ ) and a higher degree of crystallization. This is because, during the deposition, oxygen has time to integrate into the crystal lattice vacancies and initiate the process of material crystallization, whereas in our case it appears in the form of embedded oxygen outside the crystal lattice. Annealing at a controlled temperature gave certain energy for oxygen activation, which brought the film to certain values of the carrier concentration:  $N_c$  in the range from 1 to  $10 \cdot 10^{20} \text{ cm}^{-3}$ . Moreover, as described above, crystallization occurs due to oxygen channels that are formed in the film.

**Electro-optical modulation.** We fabricate MOS capacitors (Si/SiO<sub>2</sub>/ITO/Me, Fig. 4a) based on ITO films 1, 2, 3 with aluminum (Al, work function is 4.2 eV) and silver (Ag, 4.8 eV) electrodes. MOS capacitors with Al electrodes demonstrate the breakdown voltage of less than 20 mV (Fig. 4b, red vertical curve). When replacing Al electrode to Ag one, a significantly higher breakdown voltage of 17 V can be observed with the leakage current of less than 5 nA (Fig. 4b, blue curve). Whereas MOS capacitor without electrodes (the probes contacted directly with the ITO film) showed breakdown voltage of 29 V (Fig. 4b, yellow curve). The high noise level in this case can be explained by poorer contact between the probe and ITO film surface. Based on these measurements of MOS-capacitors current-voltage characteristics we assumed that Al/ITO pair forms an energy barrier at their interface. When electrical potential is applied, an electron emission occurs due to smaller Al work function compared ITO (4.2 eV versus 4.7 eV, respectively – Fig. 4a – the targeted area). That means 0.5 eV energy barrier ( $\Delta\phi_{ms} = \Phi_{ITO} - \Phi_{Al}$ ) is appeared at Al / ITO interface. The emission current density in this case is defined as:

$$j = j_{ITO \rightarrow Al} - j_{Al \rightarrow ITO} = q n_s v_0 (e^{\beta V_g} - 1), \quad (1)$$

where  $q$  is an electron charge,  $n_s = n_0 e^{-\beta \Delta \phi}$  – surface concentration in a semiconductor/metal interface,  $\beta = q/kT$ ,  $v_0$  – thermal velocity of electrons. In this case the free path of electrons in ITO equals to 17.8 nm:

$$l_e = \frac{h}{q^2 N \lambda_e} \quad (2)$$

where  $h$  – Plank's constant,  $1/\lambda_e = (3\pi^2 N)^{1/3}$ .

The calculated electric current in this barrier for chosen electrode area (approximately 2 mm<sup>2</sup>) is about 0.19 A (at applied voltage of 20 mV – Eq. 1). Additionally, free electrons can be accelerated by an external electric field and pass through the ITO layer (the electron mean free path is comparable to the film thickness), which can lead to oxide destruction and breakdown.

Next, we investigated ITO film optical characteristics switching under applied voltage. We decided to use MOS structure without electrodes in order to achieve better sensitivity and higher applied voltage (Fig. 5a). Ellipsometry parameters  $\psi$  and  $\Delta$  were carefully measured in a wide wavelength range from 400 to 1600 nm for multilayer stacks with the ITO films<sup>13</sup>. We observe a higher influence of the applied voltage on  $\psi$  and  $\Delta$  at longer wavelengths in the range from 1400 to 1600 nm (Fig. 5c, d). The dependencies of the applied voltage (data validation was performed only from 0 to +3 V for the film 3) on ellipsometry characteristics ( $\psi$ ,  $\Delta$ ) were measured at a standard telecom wavelength of 1550 nm (Fig. 5b).

The change in the film<sup>1</sup> ellipsometry parameters is found to be lower compared with the film<sup>2</sup>, despite the fact these films have close values of the carrier concentration. Presumably, this can be explained by the presence of electron traps in the less crystallized structure of film<sup>1</sup>, which prevents the charge accumulation. The film<sup>3</sup> possesses the strongest electro-optical effect because of the highest carrier concentration value. Based on carried measurements we studied ITO thin film optical parameters (see Supplementary). The complex refractive index of the accumulation layer was calculated using the

Drude-Lorentz model in the wavelength range from 550 to 1600 nm (Fig. 5e). We compared  $\Delta n$  and  $\Delta k$  for different ITO films at a wavelength of 1550 nm (Table 2, for details see Supplementary). The refractive index change for them is several times less than was mentioned in the recent works (Table 3). We assume, that this is the result of a big millimeter-scale electrode area which leads to weaker accumulation (depletion) in the ellipsometer spot area, because the charge coming from the probe distributes unevenly. Finally, we calculated (see Supplementary), that such device implementation can potentially provide an electro-optical modulation frequency of approximately 5 GHz (with silver electrodes

placed on top of the ITO layer). In further work, we suppose device implementation with single-crystalline Ag electrode [37, 38], which could abate losses induced by SPP propagation at electrode interfaces.

Table 2  
Comparison of refractive index and extinction coefficient change for the various ITO films at  $\lambda = 1550$  nm.

| <b>parameter</b>             | <b>film 1</b> | <b>film 2</b> | <b>film 3</b> |
|------------------------------|---------------|---------------|---------------|
| $\Delta n$ (+ 16 V)          | 0.053         | 0.048         | 0.101         |
| $\Delta n$ (-16 V)           | 0.030         | 0.053         | 0.098         |
| $\Delta k$ (+ 16 V)          | 0.030         | 0.028         | 0.119         |
| $\Delta k$ (-16 V)           | 0.016         | 0.056         | 0.121         |
| <b><math>\Delta n</math></b> | <b>0.083</b>  | <b>0.101</b>  | <b>0.199</b>  |
| <b><math>\Delta k</math></b> | <b>0.046</b>  | <b>0.084</b>  | <b>0.240</b>  |
| n (at 0V)                    | 1.342         | 1.308         | 0.675         |
| k (at 0V)                    | 0.226         | 0.141         | 0.329         |

Table 3  
Comparison of device parameters and ITO characteristics in recent works related to electro-optical modulation.

| Device parameters                    |        |                          | ITO characteristics     |                       |                                   |                               |                               |                                |                                |
|--------------------------------------|--------|--------------------------|-------------------------|-----------------------|-----------------------------------|-------------------------------|-------------------------------|--------------------------------|--------------------------------|
| Device                               | IL, dB | L <sub>device</sub> , um | V <sub>switch</sub> , V | t <sub>ITO</sub> , nm | N <sub>c</sub> , cm <sup>-3</sup> | n <sub>ITO</sub><br>(1550 nm) | k <sub>ITO</sub><br>(1550 nm) | Δn <sub>ITO</sub><br>(1550 nm) | Δk <sub>ITO</sub><br>(1550 nm) |
| Electroabsorption design             |        |                          |                         |                       |                                   |                               |                               |                                |                                |
| [3]                                  | 1      | 5                        | ± 5                     | 10                    | 1.1·10 <sup>19</sup>              | 1.964<br><b>(1310 nm)</b>     | 0.002<br><b>(1310 nm)</b>     | 0.922<br><b>(1310 nm)</b>      | 0.271<br><b>(1310 nm)</b>      |
| [36]                                 | -      | 1700                     | - 5                     | 50                    | 1.87·10 <sup>20</sup>             | 1.75                          | 0.195                         | 0.08                           | 0.075                          |
| Mach-Zehnder design                  |        |                          |                         |                       |                                   |                               |                               |                                |                                |
| [13]                                 | 6      | 32                       | ± 6                     | 10                    | 2.29·10 <sup>20</sup>             | 1.45                          | 0.18                          | ~ 1                            | -                              |
| [37]                                 | -      | 2                        | ± 16                    | 10                    | 2.3·10 <sup>20</sup>              | 1.62                          | 0.15                          | 0.15                           | 0.1                            |
| [27]                                 | 6      | 1.5                      | ± 13                    | 10                    | 3.13·10 <sup>20</sup>             | 1.44                          | 0.12                          | 0.44                           | 0.11                           |
| MOS-stack ellipsometry investigation |        |                          |                         |                       |                                   |                               |                               |                                |                                |
| [23]                                 | -      | -                        | + 5                     | 40                    | 3.63·10 <sup>20</sup>             | 0.8                           | 0.25                          | 0.02                           | 0.015                          |
| Our work                             | -      | -                        | ± 16                    | 20                    | 3.79·10 <sup>20</sup>             | 1.31                          | 0.14                          | 0.1                            | 0.084                          |

## Summary And Conclusions

In conclusion, we developed the thin ITO films deposition technique using ion-beam assisted e-beam evaporation with the following annealing for the electro-optical signal modulation devices. With the proposed technique we deposited ultra-flat (RMS surface roughness from 0.6 to 0.8 nm) 20 nm-thick ITO films with a low carrier concentration up to  $1 \cdot 10^{20} \text{ cm}^{-3}$ . We demonstrated the direct dependencies of the thin ITO films resistivity on their crystalline structure. Scanning electron microscopy and EBSD analysis allowed us to propose a mechanism of the putative oxygen diffusion channels arising during the crystallization of the films prepared with IBAD, which is the result of the growing  $\text{In}_2\text{O}_3$  nucleus crystalline phase during deposition. Then, we designed and fabricated MOS-structure based on ITO thin films stack with high breakdown voltage of 17 to 29 V for ITO-based electro-optical modulator active elements. We experimentally demonstrated that one of the decisive factors defining MOS-structure electrical characteristics was the proper electrode material choice. Using the silver electrode in the MOS-structure leads to significantly higher breakdown voltage compared to the aluminum electrode. Finally, we

observed strong electro-optical modulation of the complex refractive index ( $\Delta n = 0.199$ ,  $\Delta k = 0.240$ ) at a wavelength of 1550 nm in a voltage range from +16 to -16 V. These results demonstrate the possibility to create integrated GHz-range electro-optical modulators with low propagation losses (theoretically estimated losses are less than 4 dB without device design optimization).

## Declarations

### Acknowledgements

Samples were made and measured at the BMSTU Nanofabrication Facility (FMN Laboratory, FMNS REC, ID 74300).

### Author contributions statement

E.S.L., A.S.B., I.A.R. (Ilya A. Ryzhikov) and I.R. (Ilya A. Rodionov) conceptualized the ideas of the project. E.S.L. performed device simulation, optimization of the thin films stack and the device parameters. E.S.L. fabricated thin films and devices. O.S.S., E.S.L., I.A.R., A.S.B. and I.R. performed morphology characterization and discussed microscopy/diffraction results. E.S.L., A.V.Z. and I.A.R. conducted the electrical characterization of the experimental stacks. E.S.L., I.V.B., A.I.I. and A.V.B. conducted characterization of the thin films optical parameters and electro-optical modulation. E.S.L., I.A.R. and A.S.B. prepared writing-original draft. I.R. reviewed and edited the manuscript. I.R. supervised the project. All authors analyzed the data and contributed to writing the manuscript.

### Additional information

The authors declare no conflict of interest.

## References

1. Poulton, C. V. *et al.* Coherent solid-state LIDAR with silicon photonic optical phased arrays. *Optics letters*, **42**, 4091–4094 <https://doi.org/10.1364/OL.42.004091> (2017).
2. Baburin, A. S. *et al.* Highly directional plasmonic nanolaser based on high-performance noble metal film photonic crystal. *Nanophotonics VII*, **10672**, <https://doi.org/10.1117/12.2307572> (2018).
3. Cheng, Q., Rumley, S., Bahadori, M. & Bergman, K. Photonic switching in high performance datacenters. *Optics express*, **26**, 16022–16043 <https://doi.org/10.1364/OE.26.016022> (2018).
4. Amin, R. *et al.* ITO-based electro-absorption modulator for photonic neural activation function. *APL Materials*, **7**, 081112 <https://doi.org/10.1063/1.5109039> (2019).
5. Shastri, B. J. *et al.* Photonics for artificial intelligence and neuromorphic computing. *Nat. Photonics*, **15**, 102–114 <https://doi.org/10.1038/s41566-020-00754-y> (2021).
6. Wang, C. *et al.* Integrated lithium niobate electro-optic modulators operating at CMOS-compatible voltages. *Nature*, **562**, 101–104 <https://doi.org/10.1038/s41586-018-0551-y> (2018).

7. Witmer, J. *et al.* High-Q photonic resonators and electro-optic coupling using silicon-on-lithium-niobate. *Sci Rep*, **7**, 46313 <https://doi.org/10.1038/srep46313> (2017).
8. Green, W. M., Rooks, M. J., Sekaric, L. & Vlasov, Y. A. Ultra-compact, low RF power, 10 Gb/s silicon Mach-Zehnder modulator. *Optics express*, **15**, 17106–17113 <https://doi.org/10.1364/OE.15.017106> (2007).
9. Xiao, X. *et al.* High-speed, low-loss silicon Mach–Zehnder modulators with doping optimization. *Optics express*, **21**, 4116–4125 <https://doi.org/10.1364/OE.21.004116> (2013).
10. Haffner, C. *et al.* Low-loss plasmon-assisted electro-optic modulator. *Nature*, **556**, 483–486 <https://doi.org/10.1038/s41586-018-0031-4> (2018).
11. Palmer, R. *et al.* Low power Mach–Zehnder modulator in silicon-organic hybrid technology. *IEEE Photonics Technology Letters*, **25**, 1226–1229 <https://doi.org/10.1109/LPT.2013.2260858> (2013).
12. Paul, K. L. *et al.* Design and fabrication of InGaAsP/InP waveguide modulators for microwave applications. *Optical Technology for Microwave Applications VI and Optoelectronic Signal Processing for Phased-Array Antennas III* **1703**, International Society for Optics and Photonics; <https://doi.org/10.1117/12.138398> (1992).
13. Sorger, V. J., Lanzillotti-Kimura, N. D., Ma, R. M. & Zhang, X. Ultra-compact silicon nanophotonic modulator with broadband response. *Nanophotonics*, **1**, 17–22 <https://doi.org/10.1515/nanoph-2012-0009> (2012).
14. Li, E., Gao, Q., Chen, R. T. & Wang, A. X. Ultracompact silicon-conductive oxide nanocavity modulator with 0.02 lambda-cubic active volume. *Nano letters*, **18**, 1075–1081 <https://doi.org/10.1021/acs.nanolett.7b04588> (2018).
15. Amin, R. *et al.* 0.52 V mm ITO-based Mach-Zehnder modulator in silicon photonics. *APL Photonics*, **3**, 126104 <https://doi.org/10.1063/1.5052635> (2018).
16. Amin, R. *et al.* Heterogeneously integrated ITO plasmonic Mach–Zehnder interferometric modulator on SOI. *Sci Rep*, **11**, 1287 <https://doi.org/10.1038/s41598-020-80381-3> (2021).
17. Tahersima, M. H. *et al.* Coupling-enhanced dual ITO layer electro-absorption modulator in silicon photonics. *Nanophotonics*, **8**, 1559–1566 <https://doi.org/10.1515/nanoph-2019-0153> (2019).
18. Cleary, J. W., Smith, E. M., Leedy, K. D., Grzybowski, G. & Guo, J. Optical and electrical properties of ultra-thin indium tin oxide nanofilms on silicon for infrared photonics. *Optical Materials Express*, **8**, 1231–1245 (2018).
19. Amin, R. *et al.* Active material, optical mode and cavity impact on nanoscale electro-optic modulation performance. *Nanophotonics*, **7**, 455–472 <https://doi.org/10.1364/OME.8.001231> (2017).
20. Ma, Z., Li, Z., Liu, K., Ye, C. & Sorger, V. J. Indium-tin-oxide for high-performance electro-optic modulation. *Nanophotonics*, **4**, 198–213 <https://doi.org/10.1515/nanoph-2015-0006> (2015).
21. Feigenbaum, E., Diest, K. & Atwater, H. A. Unity-order index change in transparent conducting oxides at visible frequencies. *Nano letters*, **10**, 2111–2116 <https://doi.org/10.1021/nl1006307> (2010).

22. Xian, S. *et al.* Effect of oxygen stoichiometry on the structure, optical and epsilon-near-zero properties of indium tin oxide films. *Optics express*, **27**, 28618–28628 <https://doi.org/10.1364/OE.27.028618> (2019).
23. Lee, H. W. *et al.* Nanoscale conducting oxide PlasMOSfor. *Nano letters*, **14**, 6463–6468 <https://doi.org/10.1021/nl502998z> (2014).
24. Gui, Y. *et al.* Towards integrated metatronics: a holistic approach on precise optical and electrical properties of Indium Tin Oxide. *Sci Rep*, **9**, 11279 <https://doi.org/10.1038/s41598-019-47631-5> (2019).
25. Rajput, S. *et al.* Optical modulation in hybrid waveguide based on Si-ITO heterojunction. *Journal of Lightwave Technology*, **38**, 1365–1371 <https://doi.org/10.1109/JLT.2019.2953690> (2019).
26. Meng, L. J., Teixeira, V. & Dos Santos, M. P. Effect of the deposition rate on ITO thin film properties prepared by ion beam assisted deposition (IBAD) technique. *physica status solidi (a)*, **207**, 1538–1542 <https://doi.org/10.1002/pssa.200983704> (2010).
27. Sytchkova, A. *et al.* Depth dependent properties of ITO thin films grown by pulsed DC sputtering. *Materials Science and Engineering: B*, **178**, 586–592 <https://doi.org/10.1016/j.mseb.2012.11.010> (2013).
28. Ali, H. M., Mohamed, H. A. & Mohamed, S. H. Enhancement of the optical and electrical properties of ITO thin films deposited by electron beam evaporation technique. *The European Physical Journal Applied Physics*, **31**, 87–93 <https://doi.org/10.1051/epjap:2005044> (2005).
29. Inerbaev, T. M., Sahara, R., Mizuseki, H., Kawazoe, Y. & Nakamura, T. Interstitial oxygen and dopant atoms arrangement in tin-doped indium oxide. *Materials transactions*, **48**, 666–669 <https://doi.org/10.2320/matertrans.48.666> (2007).
30. Hou, Q. *et al.* A. Defect formation in In<sub>2</sub>O<sub>3</sub> and SnO<sub>2</sub>: A new atomistic approach based on accurate lattice energies. *Journal of Materials Chemistry C*, **6**, 12386–12395 <https://doi.org/10.1039/C8TC04760J> (2018).
31. Buckeridge, J. *et al.* Deep vs shallow nature of oxygen vacancies and consequent n-type carrier concentrations in transparent conducting oxides. *Physical Review Materials*, **2**, 054604 <https://doi.org/10.1103/PhysRevMaterials.2.054604> (2018).
32. Liu, C., Matsutani, T., Asanuma, T. & Kiuchi, M. Structural, electrical and optical properties of indium tin oxide films prepared by low-energy oxygen-ion-beam assisted deposition. *Nuclear Instruments and Methods in Physics Research Section B: Beam Interactions with Materials and Atoms*, **206**, 348–352 [https://doi.org/10.1016/S0168-583X\(03\)00760-2](https://doi.org/10.1016/S0168-583X(03)00760-2) (2003).
33. Vasudev, A. P., Kang, J. H., Park, J., Liu, X. & Brongersma, M. L. Electro-optical modulation of a silicon waveguide with an “epsilon-near-zero” material. *Optics express*, **21**, 26387–26397 <https://doi.org/10.1364/OE.21.026387> (2013).
34. Rajput, S. *et al.* Optical Modulation via Coupling of Distributed Semiconductor Heterojunctions in a Si-ITO-Based Subwavelength Grating. *Phys. Rev. Applied*, **15**, 054029 <https://doi.org/10.1103/PhysRevApplied.15.054029> (2021).

35. Li, H. *et al.* High temperature conductive stability of indium tin oxide films. *Frontiers in Materials*, **7**, 113 <https://doi.org/10.3389/fmats.2020.00113> (2020).
36. Kühnle, J., Bergmann, R. B., Krinke, J. & Werner, J. H. Comparison of vapor phase and liquid phase epitaxy for deposition of crystalline Si on glass. *MRS Online Proceedings Library (OPL)* **426**; <https://doi.org/10.1557/PROC-426-111> (1996).
37. Baburin, A. S. *et al.* Crystalline structure dependence on optical properties of silver thin film over time. *In 2017 Progress in Electromagnetics Research Symposium-Spring (PIERS)*, 1497–1502. IEEE; 10.1109/PIERS.2017.8261984 (2017).
38. Rodionov, I. A. *et al.* Mass production compatible fabrication techniques of single-crystalline silver metamaterials and plasmonics devices. *In Metamaterials, Metadevices, and Metasystems*, **10343**, <https://doi.org/10.1117/12.2271643> (2017).
39. Quaas, M., Steffen, H., Hippler, R. & Wulff, H. Investigation of diffusion and crystallization processes in thin ITO films by temperature and time resolved grazing incidence X-ray diffractometry. *Surface science*, **540**, 337–342 [https://doi.org/10.1016/S0039-6028\(03\)00850-1](https://doi.org/10.1016/S0039-6028(03)00850-1) (2003).
40. Rodionov, I. A. *et al.* Quantum Engineering of Atomically Smooth Single-Crystalline Silver Films. *Sci Rep*, **9**, 12232 <https://doi.org/10.1038/s41598-019-48508-3> (2019).

## Figures

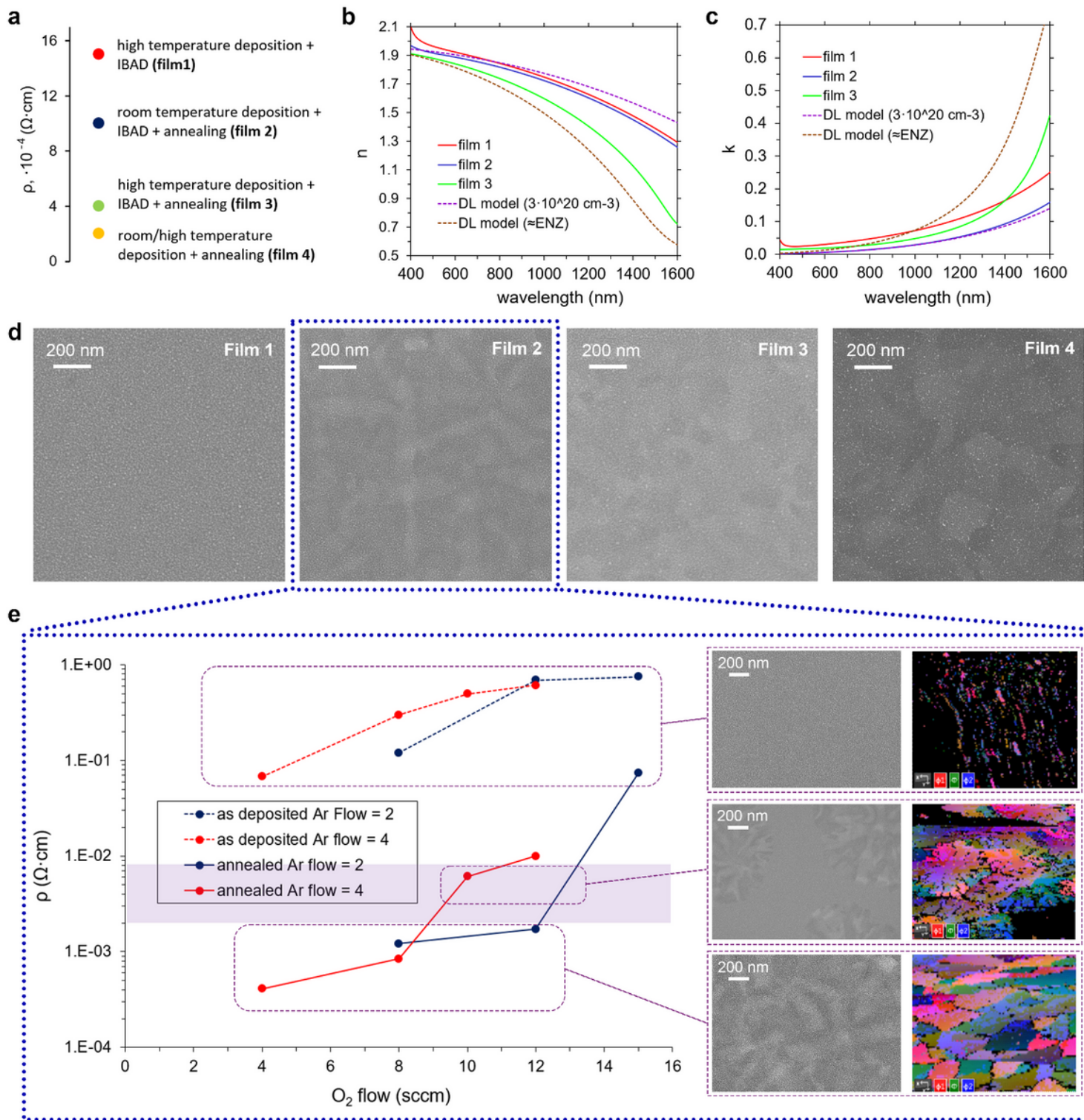


**Figure 1**

(a) ITO films resistivity via deposition technique; ITO films (b)  $n$  and (c)  $k$  dependence on wavelength; (d) SEM images of the ITO films surface; (e) Resistivity dependence on IBAD Ar and  $\text{O}_2$  flows. Selected areas shows surfaces structure (SEM images) and crystallography (EBSD maps) of the films with different resistivity values.

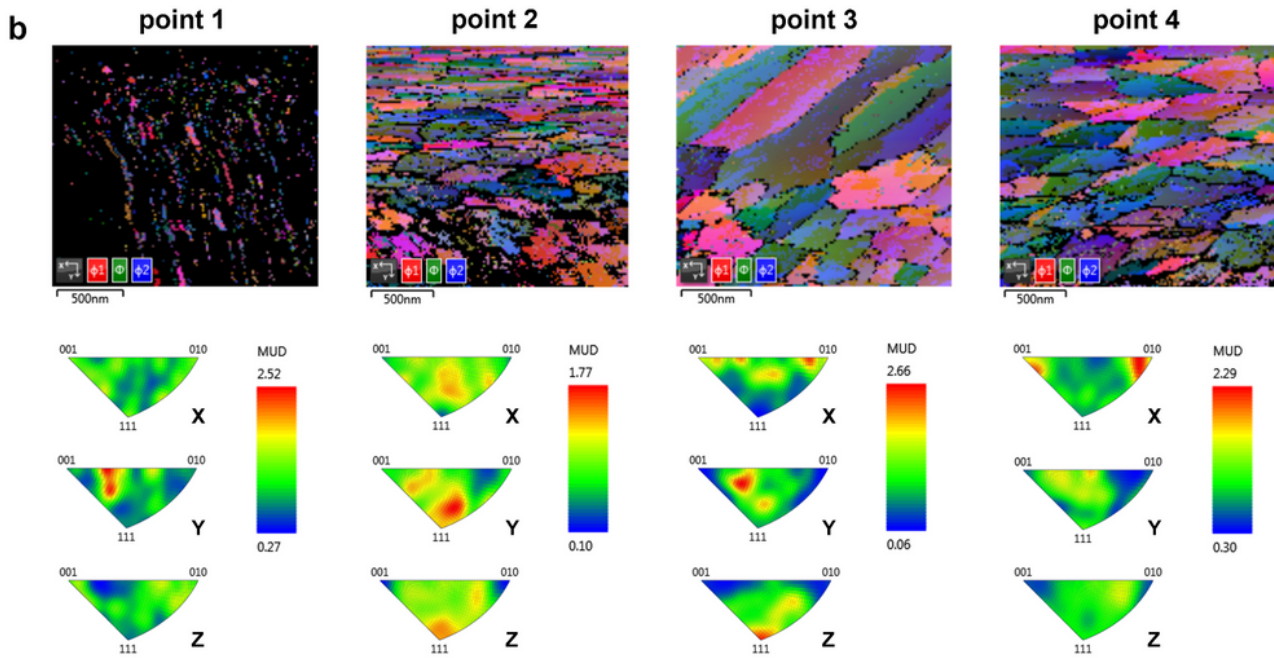
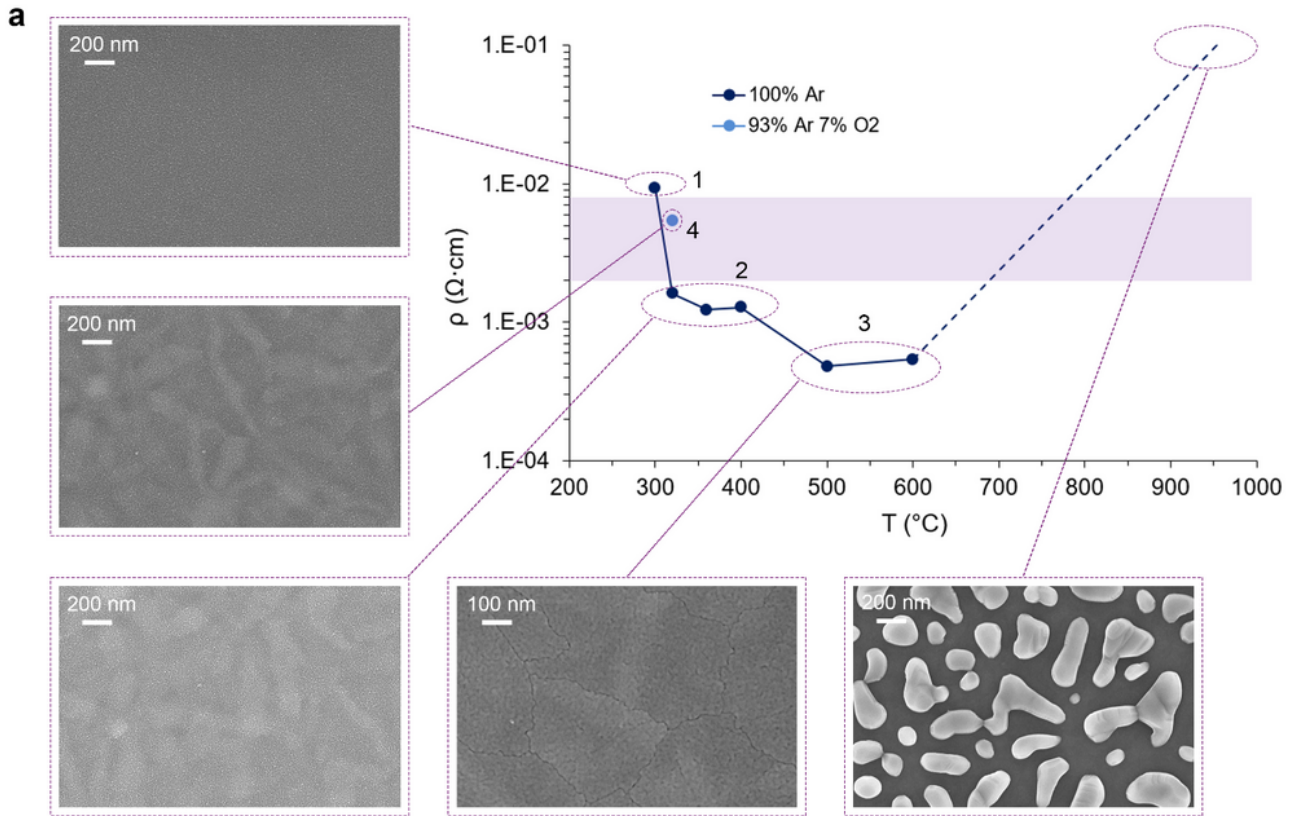


**Figure 2**

(a) Resistivity dependence on annealing temperature and annealing atmosphere; (b) EBSD analysis results.

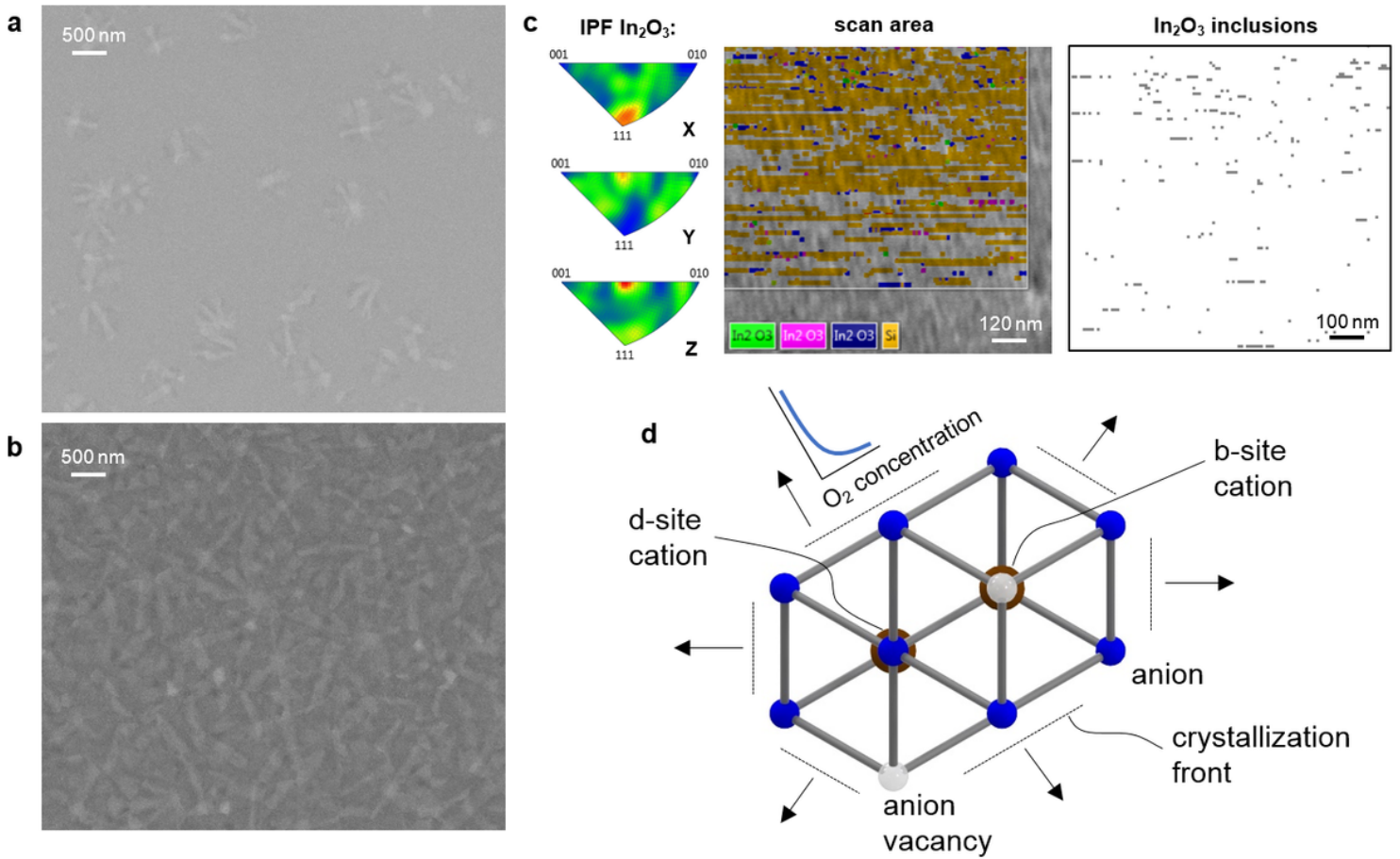


**Figure 3**

(a), (b) SEM image of the annealed crystalline ITO films; (c) EBSD analyze of not annealed ITO film deposited with IBAD, where it can be see nucleus of  $\text{In}_2\text{O}_3$  crystalline phase; (d) ITO lattice projection on  $\langle 222 \rangle$  and the crystallization process (oxygen diffusion is occurring along the direction of the crystallization front).

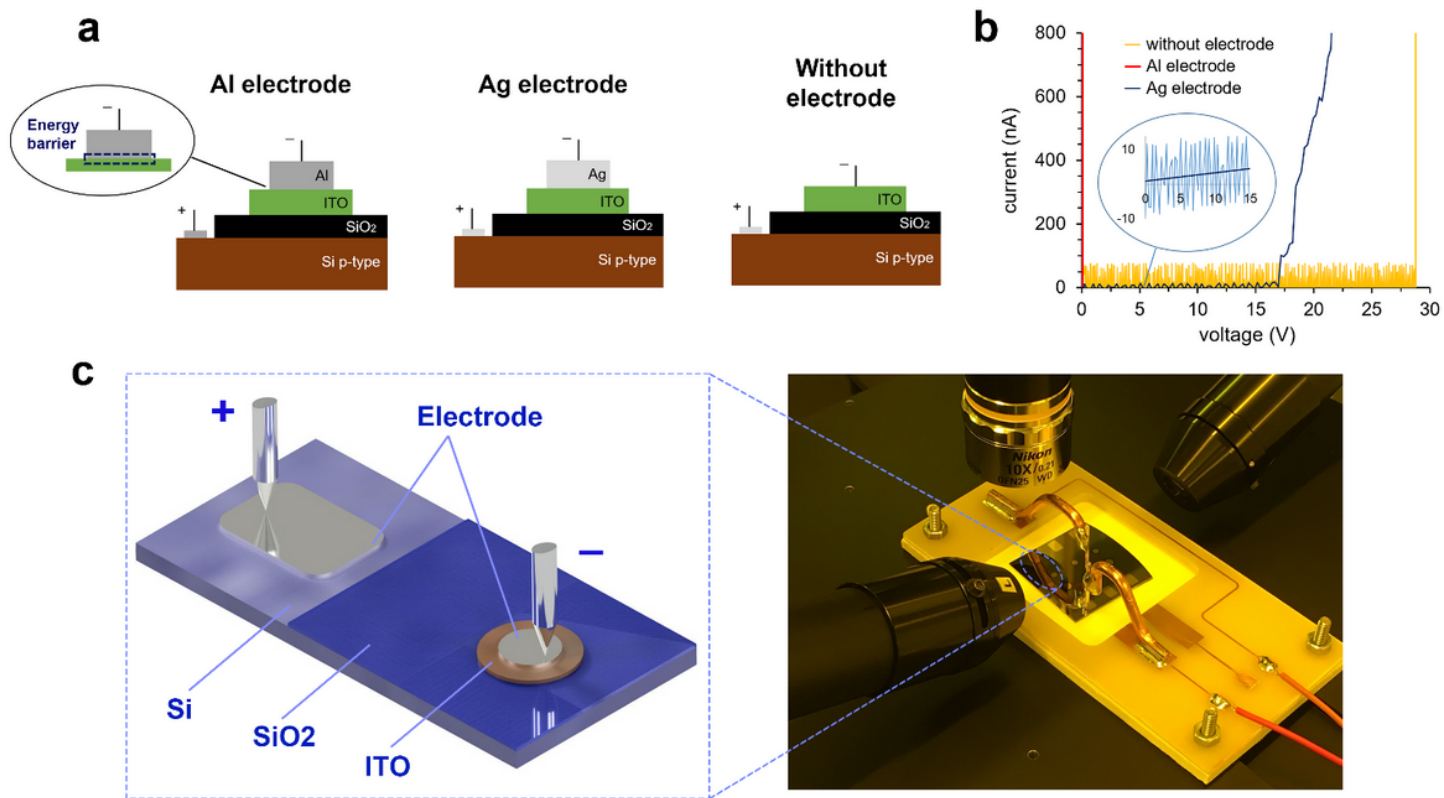


**Figure 4**

(a) Electrical characteristics measurement schemes (on the targeted area the breakdown physical model is shown); (b) Volt-ampere characteristics of the MOS capacitors; (c) Result measurement scheme set up.

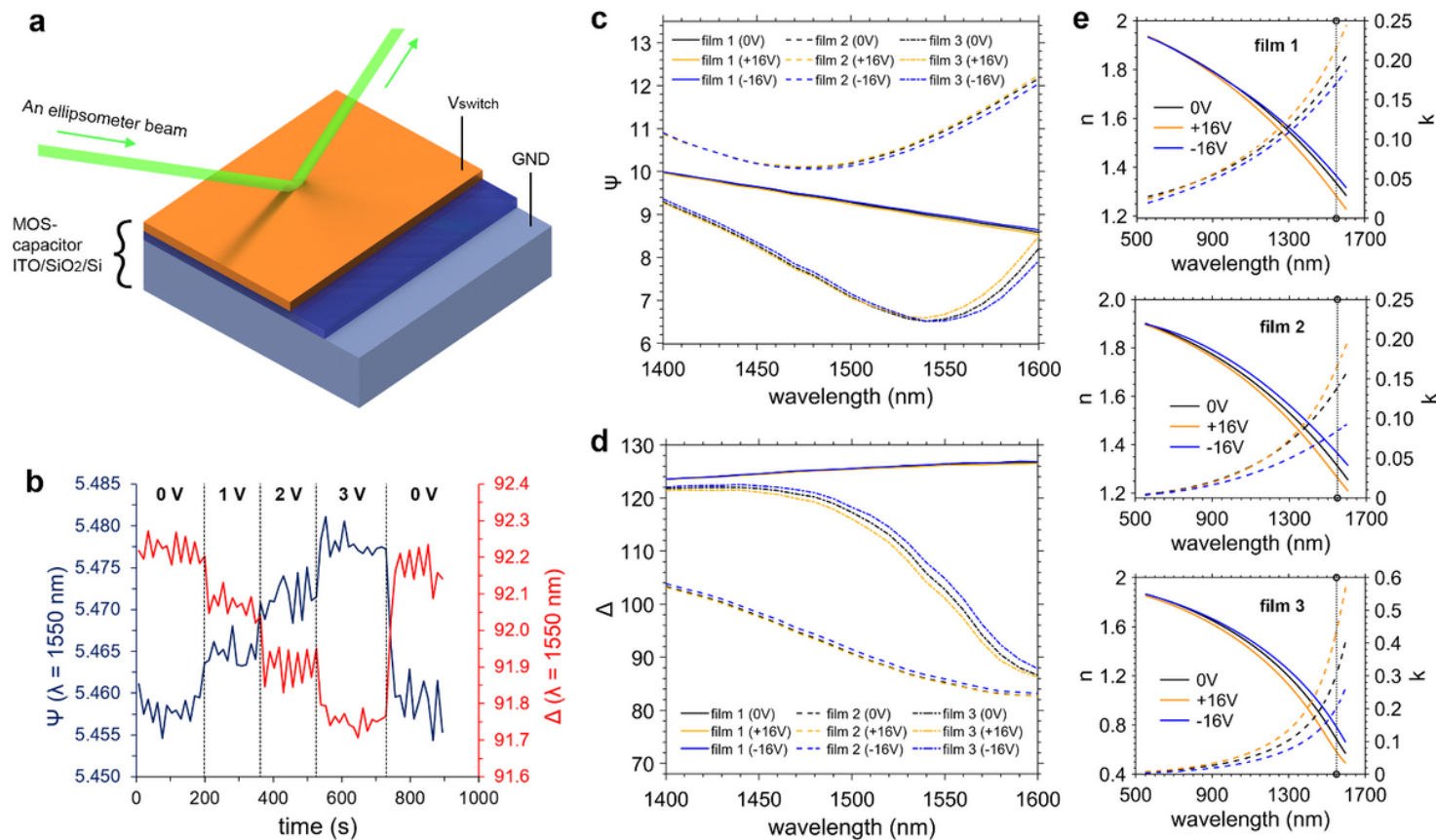


**Figure 5**

(a) A measurement scheme; (b) ITO (film 3)  $\psi$  and  $\Delta$  at wavelength of 1550 nm; (c)  $\psi$ ; (d)  $\Delta$  of the multilayer stack in the wavelength range from 1400 to 1600 nm at voltages of -16 V and +16 V; (e) film 1, 2, 3 accumulation layer  $n$  and  $k$  in the wavelength range from 550 to 1600 nm at voltages of 0, +16 and -16 V.

## Supplementary Files

This is a list of supplementary files associated with this preprint. Click to download.

- [manuscriptsupp.docx](#)